DTU Library

Modeling the Use of an Electrical Heating System to Actively Protect Asphalt Pavements against Low-temperature Cracking

Adam, Quentin Félix; Levenberg, Eyal; Ingeman-Nielsen, Thomas; Skar, Asmus

Modeling the use of an electrical heating system to actively protect asphalt pavements against low-temperature cracking

Quentin Félix Adam [*], Eyal Levenberg, Thomas Ingeman-Nielsen, Asmus Skar

Technical University of Denmark (DTU), Nordvej 119, Kongens Lyngby 2800, Denmark

ARTICLE INFO

ABSTRACT

This paper addressed the case of an electrically heated asphalt pavement; it explored an unconventional application of such a system – not for combating snow and ice – but for mitigating low-temperature cracking. The investigation was done *in silico*, considering a stratified medium to represent the asphalt pavement system, a thin heat-generating layer to represent the heating system, and measured weather conditions from Greenland to emulate a cold region that can potentially produce thermal cracking. A thermomechanical model was outlined, consisting of a one-dimensional thermal formulation that accounts (also) for latent heat effects, and a three-dimensional mechanical formulation based on linear viscoelasticity that assumes thermo-rheological simplicity. A cold-weather event, leading to a thermal crack, was identified by the thermomechanical model. Additionally, a parametric investigation was carried out to quantify the effects of the heating system's embedment depth and heating production on the activation timing needed to prevent cracking. It is found that mitigating low-temperature cracking with an embedded electric heating system is attainable and workable. Doing so is most effective when the heating system resides close to the ride surface. A procedure for automatic heating operation was proposed for practical implementation.

1. Introduction

1.1. Background

Asphalt pavements in cold regions are prone to low-temperature cracking; this distress is manifested by transverse cracks that appear after an isolated event of fast cooling in combination with low-temperature levels, or due to several cooling cycles that ultimately produce a macro crack. In general terms, due to their large lateral extent, asphalt layers are restrained from horizontally contracting or expanding. Therefore, fluctuating temperature conditions cause a buildup of thermal stresses, either tensile or compressive. Specifically, low-temperature cracking is induced by a tensile thermal stress exceeding the layer's tensile strength (Wang, 2018) or by accumulating damage due to several tensile thermal stress repetitions, i.e. temperature fatigue cracking (Richard, 2009). This distress-type is a top-down phenomenon originating at the pavement's surface (or very near to it) (National Academies of Sciences, Engineering, and Medicine, 2010; National Academies of Sciences, Engineering, and Medicine, 2018; Canestrari and Ingrassia, 2020).

Furthermore, pavement surfaces in cold regions are exposed to weather events such as snow accumulation or ice formation (or both). These hinder user safety because of the drastic decrease in skid resistance, and also because of the masking of road markings. An emerging solution for tackling snow and ice at the ride surface of asphalt pavements is electric heating in the form of embedded ribbon elements (Sangiorgi et al., 2018), embedded cables (Liu et al., 2018), or employing conductive asphalt concrete (Rew et al., 2018). One advantage of electric heating technology is its agility, i.e. the ability to provide on-demand heat energy.

This work addresses the case of an electrically heated asphalt pavement with ribbon elements. It explores an unconventional application of such a system – not for combating snow and ice – but for mitigating low-temperature cracking. In view of the thermo-viscoelastic nature of asphalt concrete, thermal stresses are not directly linked to the prevailing temperature levels, but are linked to the entire history of temperature evolution. Thus, the analysis of low-temperature cracking must include the modeling of in-pavement temperatures under service conditions, alongside mechanistic modeling of thermally-induced failure of asphalt concrete.

---

* Corresponding author.
 E-mail address: quentin.f.adam@gmail.com (Q.F. Adam).

The paper commences with a literature review covering thermal modeling of pavements as well as analysis of low-temperature cracking. This is followed by stating the specific work objectives and methodology. Next, a thermomechanical model is presented, dealing with the case of a pavement hosting an electric heating system. Then, utilizing measured cold weather data, the model is applied to assess the possibility of mitigating low-temperature cracking by activating the heating system. Conclusions, recommendations, and future work are finally stated.

1.2. Literature review

1.2.1. Thermal modeling of pavements

The thermal modeling of pavement systems is aimed at calculating the temperature field under service for depths covering the structural layers and subgrade. The focus hereafter is on schemes that are essentially based on first principles (i.e. based on established science). One of the earliest contributions in this connection is the work of Barber (1957). The purpose of the work was to provide a calculation tool for estimating daily fluctuations of pavement temperature levels. The author proposed a closed-form solution for a half-space in contact with air at a temperature that varies as a sine having a 24 h period. Contributing weather factors were: forced convection (power law of wind speed), the intensity of shortwave solar radiation, and longwave radiation losses to the atmosphere. Calculated surface temperatures were compared with measurements; the observed differences were ascribed to inaccurate solar radiation inputs (taken from a remote location), as well as to the simplified model assumptions.

Dempsey and Thompson (1970) studied the impact of temperature-related events on layered pavements. Their objectives included: (*i*) determination of main parameters that influence the thermal field; (*ii*) development of a holistic heat-transfer model; and (*iii*) validation of the model against experimental data. Out of the wide variety of climatic effects influencing the thermal field in pavement systems, it was found that the most relevant are: air temperature, precipitation, solar radiation, and wind speed. The one-dimensional heat equation was considered with a prescribed constant temperature at a depth of about 3.6 m, and a flux balance at the surface comprised of net shortwave radiation (i.e. the difference between incoming and surface reflected radiation), net longwave radiation (i.e. the difference between incoming and emitted radiation), and air convection effects (Vehrencamp, 1953). To take into account the effects of freezing and thawing of moisture within the medium a temperature-dependent heat capacity was considered. A finite-difference solution scheme was applied to generate results over several months. Good accuracy was exhibited by the model when compared to measurements performed at two different near-surface depths. The study did not include information about choosing the initial temperature conditions within the modeled pavement. The work of Dempsey served as basis for the Enhanced Integrated Climatic Model (Dempsey et al., 1986), which integrated in-pavement moisture flow, freeze–thaw effects, with thermal analysis.

Wang et al. (2009) theoretically investigated the in-pavement thermal field; their objective was to analytically solve the heat equation in a multilayered half-space, not by imposing a temperature history at the surface, but by imposing a heat flux – represented as a linear combination of sine signals with different amplitudes and phases (i.e. Fourier series). This heat flux was based on measurements, and composed of net radiation energy and convection losses that were linearly related to the wind speed. A heat flux and temperature continuity at layer interfaces were assumed, and a bounded temperature range was forced at an infinite depth. This approach essentially superposed several steady-state solutions, which means that initial conditions did not need to be defined. In effect, the results were based on a model spin-up that involves infinite repetition of the considered inputs. Application of the method, and comparison to measured in-pavement temperatures, showed reasonable accuracy. Any discrepancies were attributed to longwave radiation emissions mainly occurring at night, which were not taken into account in the heat transfer model, and to the placement of the lower temperature boundary at an infinite depth.

The thermal modeling of pavements with embedded heating systems requires the inclusion of heat sources. In this connection, Liu et al. (2017) investigated the thermal field of small concrete slabs with embedded electric heating cables. The authors used an analytical solution for the two-dimensional heat equation that considered a single line heat source buried in a semi-infinite medium. This solution was applied to thermally mimic several heating line sources representing an array of heating cables inside a finite-size medium representing a slab. The virtual image method was employed to create adiabatic boundaries at the sides and bottom of the model; also, convection losses were applied to the surface. The model was able to reproduce 'reasonably well' the surface temperature evolution of a concrete slab exposed to varying power levels of internal heating.

Analysis of in-pavement temperature fields with internal heat sources can also be found in studies related to early-age Portland cement concrete pavements, where the hydration process serves as the heat source. McCullough and Rasmussen (1999) developed software to analyze the overall thermomechanical behavior of concrete slabs. During hydration, the concrete temperature level was considered to depend on two components: heat of hydration (influenced by e.g. the cement composition and the amount of cement), and ambient climatic effects such as air temperature, wind speed, and solar radiation. Once combined, these components provided the slab temperature level via heat exchange mechanisms. The upper boundary (i.e. the concrete slab top) was exposed to convection, shortwave and longwave radiation, while the lower boundary (i.e. the concrete slab bottom) was subjected to a zero heat flux. The two-dimensional heat equation was then considered, and solved with the finite-element method. Schindler et al. (2004) demonstrated the accuracy of this model compared to measured temperatures within two freshly constructed concrete pavements at different geographical locations.

Rainfall has generally not been included in the energy balance of the above studies. One possible reason for this is the lack of reliable measurements (Dempsey and Thompson, 1970). Nonetheless, some studies aimed at determining the effects of rain on pavement surface temperatures. Janke et al. (2009) proposed a surface energy balance taking into consideration the export of heat due to convection caused by rainfall. It was demonstrated that rain could cause a surface temperature drop of about 2 °C. With the same purpose, Van Buren et al. (2000) combined two different convection heat transfer coefficients within their heat transfer model, one for dry conditions and another for wet conditions. The latter was assumed a function of rain intensity and was set to zero during dry weather conditions.

In summary, the thermal modeling of pavement systems is achieved with different methods including closed-form solutions or approximated numerical techniques (e.g. finite-difference or finite-element methods). These methods display a common aspect: their utilization of weather effects including the shortwave solar radiation, convection effects originating from the wind speed, longwave radiations, and latent heat effects originating from freezing and thawing of moisture within structural layers.

1.2.2. Analysis of low-temperature cracking

The study of low-temperature cracking involves: (*i*) visually inspecting manifestations of this distress type for in-service asphalt pavements; (*ii*) laboratory investigations of asphalt concrete thermo-mechanical properties; and (*iii*) modeling of thermally induced stress build-up in asphalt concrete. One of the earliest scientific contributions to the subject of low-temperature cracking is the work of Hills and Brien (1966). The purpose of their work was to suggest a one-dimensional thermomechanical model for calculating thermal stresses in asphalt concrete, and then verifying the calculations by comparison against experiments. Their proposed formulation utilized an incremental

approach that linked stresses and strains via a time and temperature dependent modulus. Strains were considered to vary linearly with temperature, assuming a constant coefficient of linear thermal expansion. Different cooling rates were utilized to calculate thermal stresses. It was demonstrated that a higher cooling rate resulted in higher thermally induced stresses. Furthermore, thermal cracking was considered to occur when the stresses exceeded the tensile strength of the asphalt. The experimental work consisted of cooling asphalt concrete beam specimens at a constant rate while preventing them to contract longitudinally and recording the induced stresses. The authors' formulation was utilized to satisfactorily reproduce the measurements; also, temperatures at which fracture occurred were close to the predicted ones.

Marasteanu et al. (2007) studied the phenomenon of low-temperature cracking with mainly an experimental objective of developing laboratory fracture tests appropriate for subsequent low-temperature cracking evaluation. Different tests were performed over field-acquired and laboratory prepared specimens. These tests included measurements of: (*i*) tensile strength under thermal loading wherein specimens at 5 °C were restrained from deforming, and cooled at rate of 10 °C·hr^{-1} until fracture; and (*ii*) linear thermal expansion coefficient for both cooling and heating within the temperature range of 40 °C to −80 °C. Average tensile strengths were 2.0 MPa for field specimens, and about 2.5 MPa for laboratory specimens. In both cases strengths varied within a wide range, from a minimum of 1.0 MPa to a maximum of 6.0 MPa. These results were essentially independent of the temperature level at which fracture occurred. Also, it was observed that buildup of tensile stresses began as temperatures dropped below about zero degrees Celsius. The linear thermal expansion coefficient was observed to be temperature independent. During cooling (above −37 °C) the thermal expansion coefficient ranged from $1 \cdot 10^{-5}$ °C^{-1} to $3 \cdot 10^{-5}$ °C^{-1}. During heating (above −22 °C) the range was $3 \cdot 10^{-5}$ °C^{-1} to $5 \cdot 10^{-5}$ °C^{-1}. Field specimens exhibited similar expansion coefficient ranges.

Apeagyei et al. (2008) theoretically examined the effects of cooling rate on the thermal stresses in asphalt concrete. The objective was to show the importance of considering the cooling rate when selecting asphalt binders for design of pavements in cold regions. For this purpose, they applied the one-dimensional viscoelastic relaxation formulation, after replacing real time with reduced time, i.e. assuming time–temperature superposition (Morland and Lee, 1960). Thermal inputs included constant rates of cooling ranging from 2 °C·hr^{-1} to 10 °C·hr^{-1}. Thermomechanical material properties were based on measurements performed by Marasteanu et al. (2007), in which the asphalt concrete was characterized as a visocelastic fluid (i.e. zero long-term relaxation modulus). Reported tensile strengths were in the range of 2.2 MPa to 2.9 MPa. Calculations of tensile stress buildup commenced from zero degrees Celsius, and reported once the temperature reached −10 °C and separately once the temperature reached −30 °C. Depending on the material properties and cooling rate, the calculated tensile stresses ranged between 1.5 MPa to 3.5 MPa for the −10 °C temperature level and 2.5 MPa to 8 MPa for the −30 °C temperature level – with higher cooling rates leading to larger tensile stresses. The paper did not provide information about the numerical discretization of the viscoelastic formulation.

Judycki et al. (2015) investigated low-temperature cracking that occurred on a new highway construction in Poland. The cracks were observed to occur during a single cold weather event lasting about two weeks. The study objectives included: (*i*) field examinations, e.g. surveying of cracking; (*ii*) laboratory tests to determine mechanical properties of asphalt core specimens obtained from the highway; and (*iii*) analyses of the plausible causes for the low-temperature cracking. It was found that the cracking originated at the surface, indicating a top-down mechanism. Model-calculated thermal stresses were based on a constant cooling rate (chosen from surface temperatures acquired from nearby weather stations), and applying the method of Hills and Brien (1966) – which simplifies asphalt concrete as having a temperature-dependent modulus. Model stresses were compared to measured tensile strengths to estimate whether asphalt cracking was likely to occur. This analysis was able to reproduce the low-temperature cracking that occurred in the highway within a one degree Celsius discrepancy. This slight discrepancy was ascribed to the simplified modeling approach, and to the imprecision in the assumed temperature history, and also to the variability observed in the material modulus and tensile strength.

In summary, low-temperature cracking in asphalt pavements is studied on in-service asphalt pavements with visual inspection, in laboratory wherein thermomechanical properties of asphalt concrete are determined, and theoretically with the modeling of thermally induced stress build-up. Specifically, theoretical studies consider the quasi-elastic stress formulation from Hills and Brien (1966) or the more accurate linear viscoelastic integral equation utilized by e.g. Apeagyei et al. (2008).

1.3. Objective and methodology

This paper deals with an electrically heated asphalt pavement of the type and technology presented in Levenberg and Adam (2021); it theoretically investigates the possibility of mitigating low-temperature cracking by means of activating (i.e. switch on) the heating system. Specifically, the objectives are: (*i*) demonstrate that the overall idea is attainable and workable; (*ii*) quantify the effects of the heating system's embedment depth and heating production on the activation timing needed to prevent cracking; and (*iii*) propose an automatic procedure, applicable to any scenario, for timely activation of the heating system and for controlling the duration of operation (i.e. activation time span).

The investigation herein is done *in silico*, considering an idealized case of a one-dimensional stratified medium to represent an asphalt pavement system. The upper medium boundary, i.e. the pavement surface, is free from vehicular loadings, and subjected only to heat fluxes and convection based on measured weather data.

Low-temperature cracking is treated herein as a non load-related distress (American Society of Testing and Materials, 2020a,b). This is justified under cold temperatures because traffic-induced stresses are much smaller than the asphalt concrete's tensile strength. Also, the mechanical effects of traffic are localized in nature, confined to a small region surrounding the vehicle wheels. Moreover, for moving traffic, these effects are transient in space, and only induce short-time stress traces (when considering a given point in the pavement system). If desired, traffic effects can be considered alongside weather effects by way of superposition – as proposed in Marasteanu et al. (2004).

The heating system, composed of an array of electric ribbons, is considered as a thin heat-generating layer located at some fixed depth below the surface. A zero heat flux is imposed at a large depth to serve as a lower thermal boundary. The temperature field within the medium is calculated numerically by solving the one-dimensional heat equation utilizing an explicit finite-difference scheme. The choice for working with a one-dimensional heat formulation is justified given that weather conditions affect wide pavement areas. A more sophisticated 2-D or 3-D formulation is deemed unnecessary to achieve the stated objectives. Similarly, the choice to employ a finite-difference scheme is inconsequential for the current study; it does not exclude the possibility of working with other heat transfer software packages that are based on other computational schemes.

It is assumed that the temperature field and the resulting stress field are weakly coupled such that the latter do not affect the former (Bernd, 2010). Therefore, the heat equation is solved first, and the output is then utilized to obtain the stress conditions prevailing at the surface. The top layer, representing asphalt concrete, is taken as a linear viscoelastic solid characterized by a constant linear thermal expansion coefficient applicable to both cooling and heating conditions, and obeying a thermo-rheologically simple behavior. Therefore, the stress at the top of this layer is calculated by numerically solving the corresponding convolution integral, considering time–temperature superposition. While the

model herein does not consider changes in surface asphalt properties over time due to oxidation and radiation (Kliewer et al., 1996), the proposed formulation can remain applicable. One approach to achieve this is to expand the time–temperature superposition concept to a time–temperature-aging superposition (Ling et al., 2017).

A low-temperature crack is considered to occur (initiate) at the surface whenever it experiences a thermal stress level exceeding a pre-defined tensile strength (National Academies of Sciences, Engineering, and Medicine, 2010; Judycki et al., 2015; Canestrari and Ingrassia, 2020). After initiation, the crack propagates downward through the layer; this latter process is not modelled. For a given history of measured cold-weather data, the study objectives are pursued by investigating the possibility of thermal crack prevention. This is done *in silico* for different cases of embedment depths and heat productions, and for different activation and deactivation timing of the heating system.

2. Thermomechanical model

A thermomechanical model is formulated hereafter for a pavement system composed of three layers (see Fig. 1). The top layer (Layer 1) represents an asphalt concrete layer with thickness d_1 (m), the middle layer (Layer 2) represents an unbound granular base with thickness d_2 (m), and the bottom layer (Layer 3) represents the subgrade and deeper soil mass with thickness d_3 (m). A right-handed Cartesian coordinate system is introduced at the surface of Layer 1, with the z-axis pointing down into the medium. Accordingly, $z_1 = d_1$ denotes the depth to the interface between Layer 1 and 2, and $z_2 = d_1 + d_2$ denotes the depth to the interface between Layers 2 and 3. A thin heat-generating layer is introduced within Layer 1 at $z = z_r$ (m). The formulation is split into two parts, thermal and mechanical. The thermal formulation is concerned with solving the heat equation within the entire model medium and providing the temperature history at the top of Layer 1. The mechanical formulation is concerned with calculating thermally induced built-in stresses occurring at the top of Layer 1, for subsequent analysis of low-temperature cracking.

2.1. Thermal formulation

Assuming identical thermal properties and boundary conditions within any plane perpendicular to the z-axis, the one-dimensional heat equation was adapted for a multi-layer medium (Hickson et al., 2011). The formulation considers an internal heat source (Cannon et al., 9781) as well as the effects of moisture freezing and thawing within a layer (Guymon et al., 1984):

$$\frac{\partial}{\partial z}\left(k\frac{\partial T}{\partial z}\right) + \dot{q} = c\rho_i\frac{\partial T}{\partial t} + \rho_w L\frac{\partial \theta}{\partial t} \quad i = 1, 2, 3 \tag{1}$$

where $k = k(z,t)$ (W·m^{-1}·K^{-1}) is the effective thermal conductivity distribution, $T = T(z,t)$ (°C) is the temperature at depth z (m) at time t (s), $\dot{q}$ (W·m^{-3}) is an internal heat source representing the operation of an array of electric ribbons embedded at a depth z_r, $c = c(z,t)$ (J·kg^{-1}·K^{-1}) is the effective specific heat capacity distribution, ρ_i (kg·m^{-3}) is the bulk density of layer i, $\rho_w = 1000$ kg·m^{-3} is the density of water, $L = 335000$ J·kg^{-1} is the specific latent heat of fusion of water, and $\theta = \theta(z,t)$ (unitless) is the volumetric content of unfrozen moisture distribution within the medium; it represents the volume of moisture in a material element that is in unfrozen state divided by the bulk volume of the element.

Based on the work of Zhang et al. (2019), the volumetric content of unfrozen moisture is formulated as follows:

$$\theta = \begin{cases} \theta_i^t\left(1 - \left(\frac{-T}{273.15}\right)^{\beta_i}\right) & \text{if } T \leqslant 0\,°C \\ \theta_i^t & \text{else} \end{cases} \tag{2}$$

where β_i (unitless) is the soil moisture characteristic coefficient of layer i and θ_i^t is the total volumetric moisture content (unitless) in a material element within layer i (i.e. the volume of both frozen and unfrozen moisture in a material element divided by the bulk volume of the element); this formula accounts for the fact that not all the moisture within a layer freezes – for in-service pavements temperature levels. According to the work of Nicolsky et al. (2009), the effective thermal conductivity is calculated as a weighted geometric mean of two thermal conductivities:

$$\ln(k) = \left(1 - \frac{\theta}{\theta_i^t}\right)\ln\left(k_i^f\right) + \frac{\theta}{\theta_i^t}\ln\left(k_i^u\right) \tag{3}$$
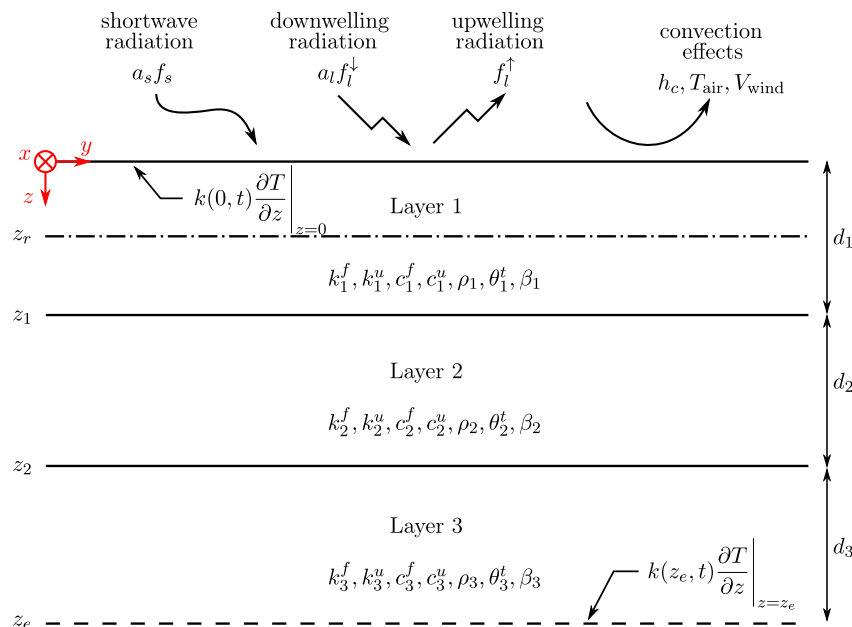

Fig. 1. Schematic cross-section of the three-layered thermal model (not to scale).

where k_i^f is the thermal conductivity of layer i at $T \leqslant 0\,°\mathrm{C}$ and k_i^u is the thermal conductivity of layer i at $T > 0\,°\mathrm{C}$. The effective heat capacity is taken as a weighted arithmetic mean of two heat capacities:

$$c = \left(1 - \frac{\theta}{\theta_i^t}\right)c_i^f + \frac{\theta}{\theta_i^t}c_i^u \tag{4}$$

where c_i^f is the heat capacity of layer i at $T \leqslant 0\,°\mathrm{C}$ and c_i^u is the heat capacity of layer i at $T > 0\,°\mathrm{C}$.

Eq. (1) is solved for an upper boundary condition consisting of an energy balance at the surface of Layer 1 (i.e. at depth $z = 0$) and a lower boundary condition consisting of a zero heat flux at a the bottom of Layer 3 (i.e. at a depth $z_e = d_1 + d_2 + d_3$). The surface energy balance is controlled by weather effects (Dempsey and Thompson, 1970). Specifically considered are convection effects, and ground level shortwave and longwave radiations. Convection effects are calculated based on Newton's law of cooling (Newton, 1701), with a heat transfer coefficient $h_c = h_c(t)$ $(\mathrm{W \cdot m^{-2} \cdot K^{-1}})$ in the form of a modified power law of the wind speed (Wolfe et al., 1983; Vehrencamp, 1953). The chosen expression takes into account both free and forced convection (Bentz, 2000):

$$h_c = \begin{cases} 5.6 + 4.0 V_{\mathrm{wind}} & \text{if } V_{\mathrm{wind}} \leqslant 5 \text{ m} \cdot \mathrm{s}^{-1} \\ 7.3 V_{\mathrm{wind}}^{0.78} & \text{else} \end{cases} \tag{5}$$

where $V_{\mathrm{wind}} = V_{\mathrm{wind}}(t)$ $(\mathrm{m \cdot s^{-1}})$ denotes wind speed. The shortwave radiation $f_s = f_s(t)$ $(\mathrm{W \cdot m^{-2}})$ originates from solar effects and contains wavelengths ranging between 0.3 µm and 2.8 µm. The longwave radiation is split into two parts, downwelling $f_l^{\downarrow} = f_l^{\downarrow}(t)$ $(\mathrm{W \cdot m^{-2}})$ and upwelling $f_l^{\uparrow} = f_l^{\uparrow}(t)$ $(\mathrm{W \cdot m^{-2}})$. Downwelling radiation originates at the sky (i.e. the atmosphere) while upwelling radiation is emitted from the surface – both are characterized by wavelengths ranging between 4.0 µm and 50 µm (Zhang et al., 2004). In the model, the shortwave radiation is weighted by the shortwave absorptivity constant of asphalt concrete $a_s = 0.9$ (unitless) reflecting the fact that a large fraction of the shortwave radiation is absorbed by the pavement (Solaimanian and Kennedy, 1993). The downwelling radiation is weighted by the pavement's surface longwave absorptivity a_l (unitless). Ultimately, the flux at surface reads:

$$-k(0,t)\frac{\partial T(z,t)}{\partial z}\bigg|_{z=0} = a_s f_s + h_c(T_{\mathrm{air}} - T(0,t)) + a_l f_l^{\downarrow} - f_l^{\uparrow}, \tag{6}$$

where $T_{\mathrm{air}} = T_{\mathrm{air}}(t)$ $(°\mathrm{C})$ is the instantaneous air temperature just above the surface.

While the downwelling radiation may be a measured entity, the upwelling radiation is typically estimated considering that the pavement surface material is behaving like a black body and applying the Stefan–Boltzmann law:

$$f_l^{\uparrow} = \sigma \varepsilon_l (T(0,t) + 273.15)^4 \tag{7}$$

where $\sigma = 5.670 \cdot 10^{-8}$ $\mathrm{W \cdot m^{-2} \cdot K^{-4}}$ is the Stefan–Boltzmann constant and ε_l (unitless) is the longwave emissivity of asphalt concrete. Given that both the downwelling and upwelling radiations operate at about the same range of wavelengths (Hartmann, 1994), and according to Kirchhoff's law of thermal radiation, the longwave absorptivity and

longwave emissivity are equal (Kirchhoff, 1860); herein $a_l = \varepsilon_l = 0.98$ (Wolfe, 1965).

The internal heat source $\dot{q}$ is located within Layer 1 (i.e. $z_r < d_1$), and represents the operation of an array of electric ribbons with heat production $w_r = w_r(t)$ $(\mathrm{W \cdot m^{-2}})$. The array of individual ribbons is smeared into a heating layer having some equivalent thickness h_{eq} (m). Consequently, the internal heat source term is expressed as follows:

$$\dot{q} = \frac{w_r(t)}{h_{\mathrm{eq}}}. \tag{8}$$

At the lower model boundary where $z = z_e$ a zero heat-flux is forced:

$$k(z_e, t)\frac{\partial T}{\partial z}\bigg|_{z=z_e} = 0. \tag{9}$$

The depth z_e is selected such that the absolute temperature variation at $z = z_e$ does not exceed some small predefined value (0.1 °C herein).

A cross-sectional view of the above-described thermal model is schematically illustrated in Fig. 1. The three layers are numbered, their associated thermal conductivities (for both $T \leqslant 0\,°\mathrm{C}$ and $T > 0\,°\mathrm{C}$), heat capacities (for both $T \leqslant 0\,°\mathrm{C}$ and $T > 0\,°\mathrm{C}$), bulk densities, total volumetric moisture contents, soil moisture characteristic coefficients, and thicknesses are noted. The different depths of interest are indicated: $z = 0$ (upper boundary), z_r (depth of internal heat source), z_1 (interface between Layers 1 and 2), z_2 (interface between Layers 2 and 3), and z_e (lower boundary). Represented with various arrows are weather effects operating at the upper boundary: absorbed shortwave radiation $a_s f_s$, absorbed downwelling radiation $a_l f_l^{\downarrow}$, upwelling radiation $f_l^{\uparrow}$, and convection effects h_c.

The solution of Eq. (1) at layer interfaces, i.e. at depths z_i $(i = 1, 2)$ requires special attention due to the sharp change in thermal properties. In order to address this issue, a heat-flux continuity between layers is prescribed (Hickson et al., 2011):

$$\frac{\partial}{\partial z}\left(k(z_i^+, t)\frac{\partial T}{\partial z}\bigg|_{z=z_i^+} - k(z_i^-, t)\frac{\partial T}{\partial z}\bigg|_{z=z_i^-}\right) = \bar{c}(z_i, t)\bar{\rho}_i\frac{\partial T}{\partial t} + \rho_w L\frac{\partial \bar{\theta}}{\partial t}, \tag{10}$$

where the subscripts z_i^+ (m) and z_i^- (m) represent depths at which temperature gradients are obtained immediately below and immediately above the interface depth, $\bar{c}(z_i, t) = 0.5c(z_i^-, t) + 0.5c(z_i^+, t)$ $(\mathrm{J \cdot kg^{-1} \cdot K^{-1}})$ is the average of the prevailing heat capacities at the above-mentioned depths, $\bar{\rho}_i = 0.5\rho_i + 0.5\rho_{i+1}$ $(\mathrm{kg \cdot m^{-3}})$ is the average of densities of layers i and $i + 1$, and $\bar{\theta} = 0.5\theta(z_i^-, t) + 0.5\theta(z_i^+, t)$ (unitless) is the average volumetric content of unfrozen moisture across the interface, i.e. considering material elements above and below z_i.

Eq. (1) was numerically solved for the entire model depth, from $z = 0$ to $z = z_e$, by means of a forward finite-difference scheme. For this purpose, the medium was discretized with a constant node spacing of $\Delta z = 0.01$ m, and time was discretized into intervals of $\Delta t = 20$ s. Based on a separate study, involving smaller node spacing combined with shorter time intervals, this choice was found to ensure stability, and balance accuracy vs. computational effort. The temperature level at every depth z and time $t + \Delta t$ is given by:

$$T(z, t + \Delta t) = \begin{cases} T(0,t) + \dfrac{2k(0,t)\Delta t}{\Delta z^2}\left(T(\Delta z, t) - T(0,t) + \dfrac{\Delta z}{k(0,t)}(a_s f_s \right. \\ \left. + h_c(T_{air} - T(0,t)) + a_l f_l^{\downarrow} - f_l^{\uparrow})\right)\left(c(0,t)\rho_1 + \rho_w L\dfrac{\partial\theta}{\partial T}\right)^{-1} & \text{if } z = 0 \\[6pt] T(z_r, t) + \Delta t\left(\dfrac{k(z_r, t)}{\Delta z^2}(T(z_r + \Delta z, t) - 2T(z_r, t)\right. \\ \left. + T(z_r - \Delta z, t)) + \dfrac{w_r(t)}{h_{eq}}\right)\left(c(z_r, t)\rho_1 + \rho_w L\dfrac{\partial\theta}{\partial T}\right)^{-1} & \text{if } z = z_r \\[6pt] T(z_i, t) + \dfrac{\Delta t}{\Delta z^2}\left(k(z_i^+, t)T(z_i + \Delta z, t) - (k(z_i^+, t) + k(z_i^-, t))T(z_i, t)\right. \\ \left. + k(z_i^-, t)T(z_i - \Delta z, t)\right)\left(\bar{c}(z_i, t)\bar{\rho}_i + \rho_w L\dfrac{\partial\theta}{\partial T}\right)^{-1} & \text{if } z = z_i (i = 1, 2) \\[6pt] T(z_e - \Delta z, t + \Delta t) & \text{if } z = z_e \\[6pt] T(z, t) + \dfrac{k(z,t)\Delta t}{\Delta z^2}(T(z + \Delta z, t) - 2T(z, t) \\ + T(z - \Delta z, t))\left(c(z,t)\rho_i + \rho_w L\dfrac{\partial\theta}{\partial T}\right)^{-1} & \text{else } (i = 1, 2, 3) \end{cases} \tag{11}$$

wherein $h_{eq} = 0.01$ m (chosen to match the node spacing) and the chain rule is applied for calculating the derivative of the volumetric unfrozen moisture content w.r.t. time (i.e. multiplying the derivative θ w.r.t. T by the derivative of T w.r.t. t). In this context, the derivative of the volumetric unfrozen moisture content θ (see Eq. (2)) w.r.t. temperature reads:

$$\frac{\partial\theta}{\partial T} = \begin{cases} -\dfrac{\theta_i^t \beta_i}{T}\left(-\dfrac{T}{273.15}\right)^{\beta_i} & \text{if } T \leqslant 0\,^\circ\text{C} \\ 0 & \text{else.} \end{cases} \tag{12}$$

2.2. Setup and initialization

The remaining model properties required to execute the thermal formulation are presented in Table 1. The table consists of three parts, each corresponding to a different model layer; it lists layer thicknesses, thermal conductivities, heat capacities, bulk densities, total volumetric moisture contents, and soil moisture characteristic coefficients. As opposed to Layers 2 and 3, fewer parameters are associated with Layer 1. This is because it represents an asphalt concrete layer assumed not to contain any moisture (i.e. $\theta_1^t = 0.0$).

Cold weather data for model execution were obtained from weather station #425000 located in Nuuk, Greenland (Cappelen, 2021). The data included hourly measurements of shortwave radiation f_s, wind speed V_{wind}, air temperature T_{air}, and relative humidity RH (%). These data were linearly interpolated to obtain values every $\Delta t = 20$s. Downwelling radiation was calculated based on air temperature and relative humidity considering the sky as a black body, and applying the Stefan–Boltzmann law:

$$f_l^{\downarrow} = \sigma\varepsilon_{sky}(T_{air} + 273.15)^4, \tag{13}$$

where $\varepsilon_{sky} = \varepsilon_{sky}(t)$ (unitless) is the sky longwave emissivity, calculated based on an empirical equation from Bliss (1961):

$$\varepsilon_{sky} = 0.8 + \frac{T_{dp}}{250} \tag{14}$$

wherein $T_{dp} = T_{dp}(t)$ (°C) is the dew point temperature level, comprised between $-20\,^\circ$C and $+30\,^\circ$C to ensure the accuracy of ε_{sky}. The dew point temperature level is determined by considering the work of

Table 1
Layer properties for the thermal model.

| Parameter	Value	Units	Description	Source
		Layer 1 – thickness $d_1 = 0.15$ m		
$k_1^f = k_1^u$	1.16	$[\text{W·m}^{-1}\text{·K}^{-1}]$	Thermal conductivity	Hassn et al. (2016)
$c_1^f = c_1^u$	964	$[\text{J·kg}^{-1}\text{·K}^{-1}]$	Heat capacity	Hassn et al. (2016)
ρ_1	2372	$[\text{kg·m}^{-3}]$	Bulk density	Hassn et al. (2016)
		Layer 2 – thickness $d_2 = 0.45$ m		
k_2^f	1.6	$[\text{W·m}^{-1}\text{·K}^{-1}]$	Thermal conductivity for $T \leqslant 0\,^\circ$C	Côté and Konrad (2005)
k_2^u	1.5	$[\text{W·m}^{-1}\text{·K}^{-1}]$	Thermal conductivity for $T > 0\,^\circ$C	Côté and Konrad (2005)
c_2^f	819	$[\text{J·kg}^{-1}\text{·K}^{-1}]$	Heat capacity for $T \leqslant 0\,^\circ$C	Andersland and Ladanyi (2003)
c_2^u	851	$[\text{J·kg}^{-1}\text{·K}^{-1}]$	Heat capacity for $T > 0\,^\circ$C	Andersland and Ladanyi (2003)
ρ_2	2081	$[\text{kg·m}^{-3}]$	Bulk density	Côté and Konrad (2005)
θ_2^t	0.03	$[-]$	Total volumetric moisture content	Côté and Konrad (2005)
β_2	0.1	$[-]$	Material characteristic coefficient	Zhang et al. (2019)
		Layer 3 – thickness $d_3 = 19.4$ m		
k_3^f	1.7	$[\text{W·m}^{-1}\text{·K}^{-1}]$	Thermal conductivity for $T \leqslant 0\,^\circ$C	Johnston (1981)
k_3^u	2.0	$[\text{W·m}^{-1}\text{·K}^{-1}]$	Thermal conductivity for $T > 0\,^\circ$C	Johnston (1981)
c_3^f	746	$[\text{J·kg}^{-1}\text{·K}^{-1}]$	Heat capacity for $T \leqslant 0\,^\circ$C	Johnston (1981)
c_3^u	900	$[\text{J·kg}^{-1}\text{·K}^{-1}]$	Heat capacity for $T > 0\,^\circ$C	Johnston (1981)
ρ_3	1950	$[\text{kg·m}^{-3}]$	Bulk density	Johnston (1981)
θ_3^t	0.05	$[-]$	Total volumetric moisture content	Johnston (1981)
β_3	0.1	$[-]$	Material characteristic coefficient	Zhang et al. (2019)
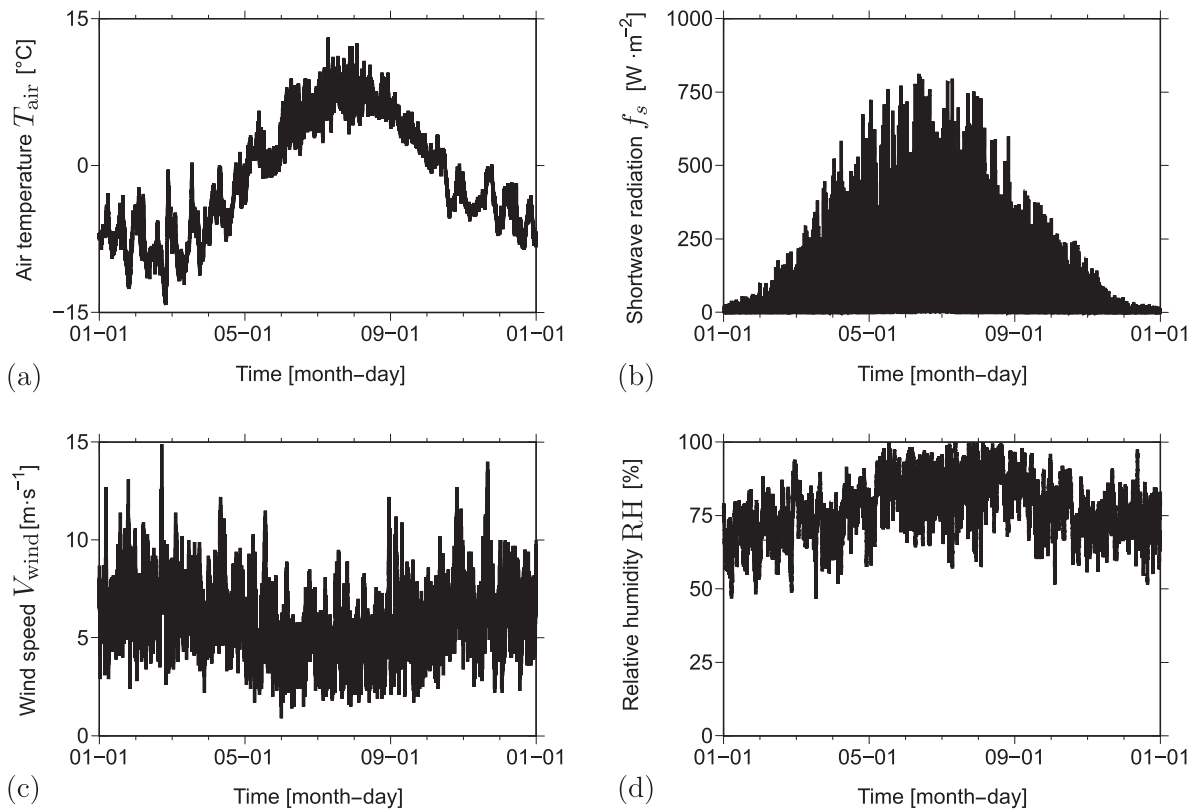
Fig. 2. Weather data of the standard year utilized for the spin-up: (a) air temperature, (b) shortwave radiation, (c) wind speed, and (d) relative humidity.

Magnus (1844) who proposed an analytical formula to calculate the saturation water vapor pressure, which is linked to T_{dp} via the relative humidity (Lawrence, 2005). Then, Bolton (1980) fitted Magnus' formula to the measured saturation water vapor pressure values of Wexler (1976) with an accuracy of 0.1%, for an air temperature range of $-30\,°C$ to $+35\,°C$ and a relative humidity comprised between 1% and 100%. The dew point temperature level is acquired with:

$$T_{dp} = 243.5 \frac{\ln\left(\frac{RH}{100\%}\right) + 17.67 \frac{T_{air}}{243.15 + T_{air}}}{17.67 - 17.67 \frac{T_{air}}{243.15 + T_{air}} - \ln\left(\frac{RH}{100\%}\right)}. \tag{15}$$

The initial temperature profile within the model medium is unknown. Therefore, the model was initialized by a so-called spin-up procedure. For this purpose a standard year was first constructed by averaging the available (hourly) weather data across the years 2014 to 2018 (both included). Second, the medium was assumed to be at a uniform temperature of 1.5 °C. Third, the model was run for 20 years by repeating the standard year weather. Finally, the thermal state obtained at the last time increment (after 20 years of analysis) was taken as the initial temperature profile for all subsequent thermomechanical calculations. A separate investigation of the spin-up procedure showed that this temperature profile is independent of the uniform temperature level assumed at the beginning.

The weather data of the standard year is presented in Fig. 2, which consists of four charts depicting the averaged measured air temperature, the shortwave radiation, the wind speed, and the relative humidity. As can be seen, the air temperature ranged approximately from $-14\,°C$ to 13 °C and remained below 0 °C for approximately 207 days. The shortwave radiation peaked at about 750 $W \cdot m^{-2}$ and 75% of the total shortwave radiation occurred between the 19th April and the 12th September, i.e. 149 days. The recorded wind speed value is taken as the arithmetic mean of the last ten minutes observations. The wind speed reached almost 15 $m \cdot s^{-1}$ and was on average 6 $m \cdot s^{-1}$. The relative humidity remained almost consistently above 50%, with an average of
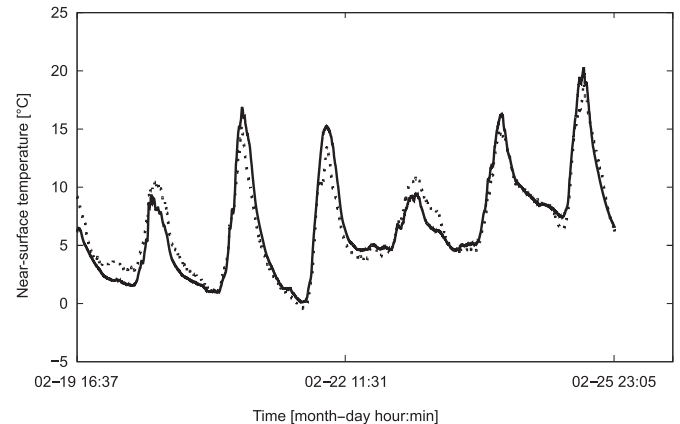

Fig. 3. Validation of the thermal code for a winter week: measured (dotted line) and calculated (solid line) temperature history at a depth of 0.01 m.

77%, and was above 90% for more than 39 days.

The thermal formulation described above was coded in ForTran 90 within a Linux environment (distribution "Linux Scientific" Version 7.7); it is freely available on GitHub (Adam, 2021a). The coding was first verified by comparison against analytic closed-form solutions involving a single thermally isotropic layer exposed at the boundaries to a prescribed temperature history and to a combination of temperature and heat-flux. The ability to account for medium layering, internal heating, and phase change due to moisture freezing and thawing, was further verified against a commercial software GeoStudio (GEO-SLOPE International Ltd., 2014) which is based on a finite-element formulation; differences were observed to be smaller than 0.13 °C (in absolute terms) for all considered cases. The latter comparison was not performed for long weather histories because GeoStudio was about two orders of

magnitude slower. Further details on the verification effort against GeoStudio are also included in the GitHub repository.

As a means of validation, the thermal code was applied in an effort to reproduce near-surface temperatures measured in an instrumented asphalt road during a winter week (Levenberg and Adam, 2021). The pavement system was essentially three-layered, comprised of (top to bottom): 0.11 m asphalt concrete layer, 0.30 m unbound aggregate base, and a local fine-grained sandy-clay soil mass extending to a large depth. The measurements were collected at one-minute intervals, yielding 9026 time-stamps in total, and included the temperature evolution at a depth of 0.01 m below the ride surface based on an average of six separate PT100 sensors. Local weather data were obtained from a slightly elevated roadside station (2 m higher than the ride surface), recording: dry-bulb air temperature, shortwave solar radiation, wind speed, and relative humidity. The model pavement system was assumed to extend to a depth of 20 m (i.e, the subgrade and deeper soil mass were assigned a thickness of 19.59 m); the thermal properties were taken from Table 1. The model was initiated with a uniform temperature profile of 7.5 °C, equal to the average air temperature during the analyzed week. This initial profile was iteratively refined (100 repetitions in total) by taking the calculated profile at the end of the week, scaling it by the ratio of the air temperature of the first minute to the air temperature of the last minute, and re-executing the code.

Fig. 3 presents model-calculated results for a depth of 0.01 m superposed over the corresponding field-measured asphalt temperatures. As can be seen, the model is able to emulate both the shape and magnitudes of the temperature history. The average absolute difference between measured and calculated temperatures is 0.93 °C, with a peak difference of 4.05 °C. These differences are rather small, especially when considering that the assumed thermal properties were not site-specific, and that the roadside weather station was not at the same elevation as the ride surface. The achieved level of reproducibility was quantified with two agreement metrics. The first was the Pearson product-moment correlation coefficient, which captures the strength of the linear dependence between two datasets, but is scale-blind (i.e., does not convey information on deviation magnitudes); a value of 0.97 was obtained indicating near-perfect correlation. The second agreement metric was the concordance correlation coefficient (Lawrence and Lin, 1989; Duveiller et al., 2016) which summarizes the closeness of two datasets, considering both correlation and scale/bias; a value of 0.96 was obtained, indicating that both the average and the standard deviation of the measured temperatures were essentially identical to the average and the standard deviation of the calculated temperatures.

2.3. Mechanical formulation

The thermomechanical model represents a pavement system with layers that extend to infinity in the x and y directions (see coordinate system in Fig. 1). Under changing temperature levels such representation prohibits deformations within any plane perpendicular to the z axis, while deformations in the z direction are unrestricted. This situation results in zero stress in the z direction, and induced thermal stresses of equal magnitude along any direction perpendicular to the z axis. The aim of the mechanical formulation is to quantify the thermal stress history $\sigma_T = \sigma_T(t)$ (MPa) at the $x - y$ plane, i.e. at the surface of Layer 1, where low-temperature cracks typically initiate.

A linear viscoelastic (solid) constitutive relation was selected for this purpose, governed by a constant Poisson's ratio $\nu_1 = 0.25$ (unitless) (Gudmarsson et al., 2015), and a thermo-sensitive relaxation modulus $E_1(t, \Delta T)$ (MPa) associated with a certain temperature level. Here, $\Delta T = \Delta T(t) = T(0,t) - T_r$ wherein T_r serves as a reference temperature for the thermal analysis. The meaning of T_r is as follows: if the material is exposed to a constant temperature level above T_r it can approach a stress-free state provided sufficient relaxation time is allowed. Conversely, if the material is exposed to a constant temperature level below T_r, induced stresses do not approach zero regardless of the

amount of relaxation time allowed.

Stress calculations were commenced from a stress-free state whenever $T(0,t) < T_r$, i.e. the surface temperature drops below the reference temperature. As long as the surface temperature remained below T_r, calculation of σ_T continues. If, at a certain time instance $T(0,t) > T_r$, i.e. the surface temperature climbs above the reference temperature, and also σ_T is tensile, the calculation of σ_T continued. However, if at a certain time instance $T(0,t) > T_r$ (i.e. the surface temperature climbs above the reference temperature) and also σ_T is compressive, the stress calculation was stopped – only to be resumed later from a stress-free state when the surface temperature again drops below the reference temperature. Herein $T_r = 0$ °C and the points in time when stress calculations are commenced are denoted by t_c (s). The values of t_c are case specific as they depend on the weather conditions and thermal model. The underlying logic for the above protocol is to indirectly account for the viscoplastic nature of asphalt concrete – as it allows for full relaxation of thermal stresses. The value of T_r is seen as a separator between a viscoelastoplastic behavior and a pure viscoelastic behavior; it is a material-dependent entity and can therefore be changed if desired.

When $E_1(t, \Delta T)$ is known, the evolution of σ_T can be calculated for a given time-history of ΔT according to the modified superposition principle (Findley and Lai, 1967). Alternatively, and perhaps more computationally efficient, is assuming thermo-rheological simplicity (Schwarzl and Staverman, 1952) which allows $\sigma_T(t)$ to be calculated according the Boltzmann superposition, as follows (Morland and Lee, 1960):

$$\sigma_T(t) = \frac{\alpha_l}{1 - \nu_1} \int_{\tau=t_c}^{\tau=t} E_1(\xi - \xi') \mathrm{d}\Delta T(\tau) \tag{16}$$

where $\alpha_l = 2 \cdot 10^{-5}$ (°C^{-1}) is the coefficient of linear thermal expansion of asphalt concrete (Islam and Tarefder, 2015; Marasteanu et al., 2007), taken herein as constant to avoid dealing with a non-linear formulation, τ (s) is a time-like integration variable ($t > t_c$), while $\xi = \xi(t)$ and $\xi' = \xi(\tau)$ are reduced (or pseudo) times (s):

$$\xi = \xi(t) = \int_{t'=t_c}^{t'=t} \frac{\mathrm{d}t'}{a_T} \text{ and } \xi' = \xi(\tau) = \int_{t'=t_c}^{t'=\tau} \frac{\mathrm{d}t'}{a_T} \tag{17}$$

in which t' (s) is also a time-like integration variable, and a_T (unitless) is the time–temperature shift factor (Schwarzl and Staverman, 1952) expressed according to the WLF equation (Williams et al., 1955):

$$\log_{10}(a_T) = \frac{-C_1 \Delta T}{C_2 + \Delta T} \tag{18}$$

where $C_1 = 30$ (unitless) and $C_2 = 200$ °C are assumed. Thus, the case of $T = T_r$ yields $a_T = 1$, and therefore $E_1(t, \Delta_T)$ is associated with the temperature level T_r. This relaxation function is taken as a four-parameter sigmoid (in double log scale):

$$E_1 = E_\infty \frac{1 + \left(\frac{t}{\tau_D}\right)^{n_D}}{\left(\frac{t}{\tau_D}\right)^{n_D} + \frac{E_\infty}{E_0}} \tag{19}$$

where $E_\infty = 400$ MPa is the long-term equilibrium modulus, $\tau_D = 10^7$ s and $n_D = 0.30$ (unitless) are shape parameters, and $E_0 = 30000$ MPa is the instantaneous modulus (Liu and Luo, 2017). A tensile strength of 2.5 MPa was assigned to Layer 1 for subsequent analyses; this choice is within the low-range of strength values reported in Marasteanu et al. (2007), Apeagyei et al. (2008).

Eq. (16) was numerically evaluated utilizing the trapezoidal integration rule (Sorvari and Hämäläinen, 2010); for this purpose t was discretized into short intervals of 60 s each. Based on a separate investigation involving shorter time intervals, this choice was verified to balance accuracy and computational effort. The coding was done in ForTran 90 and is freely available on GitHub (Adam, 2021b); it was verified by setting $E_0 = E_\infty$ and noticing that the resulting thermal stress
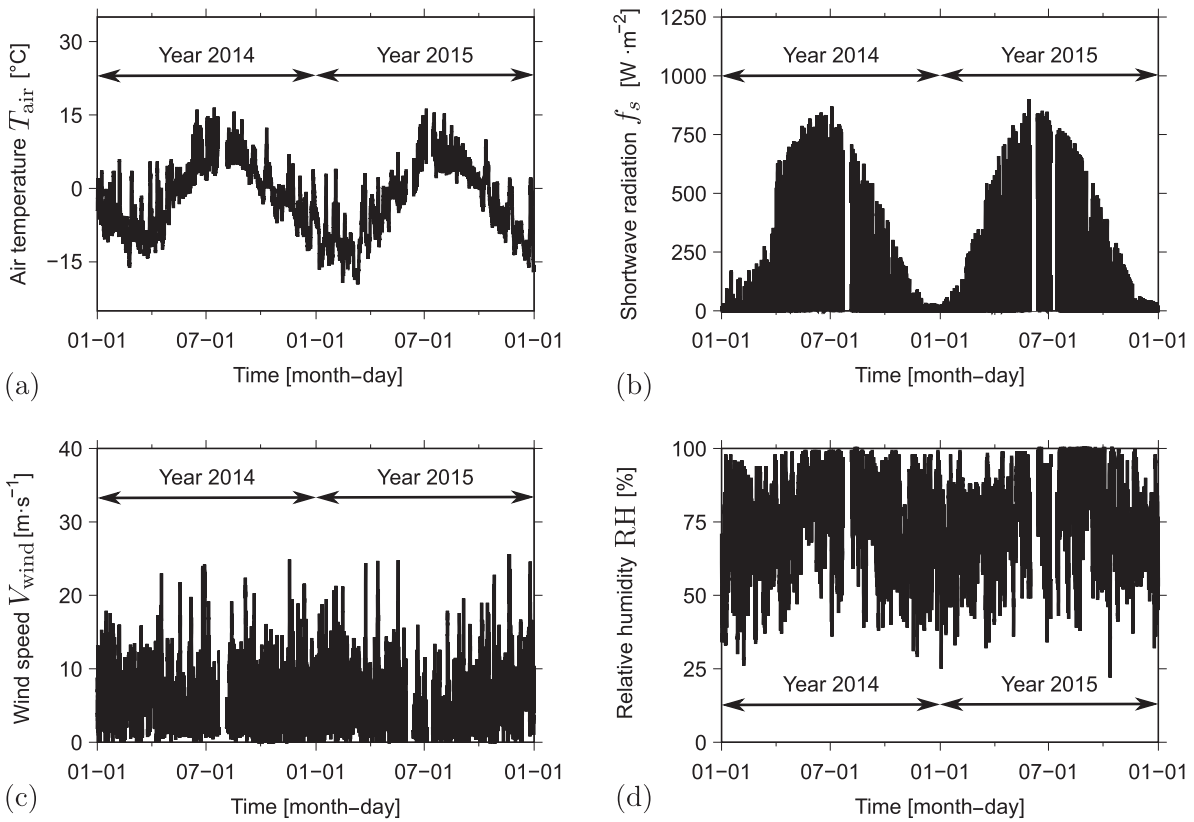
Fig. 4. Nuuk weather data for the years 2014 to 2015: (a) air temperature, (b) shortwave radiation, (c) air speed, and (d) relative humidity.
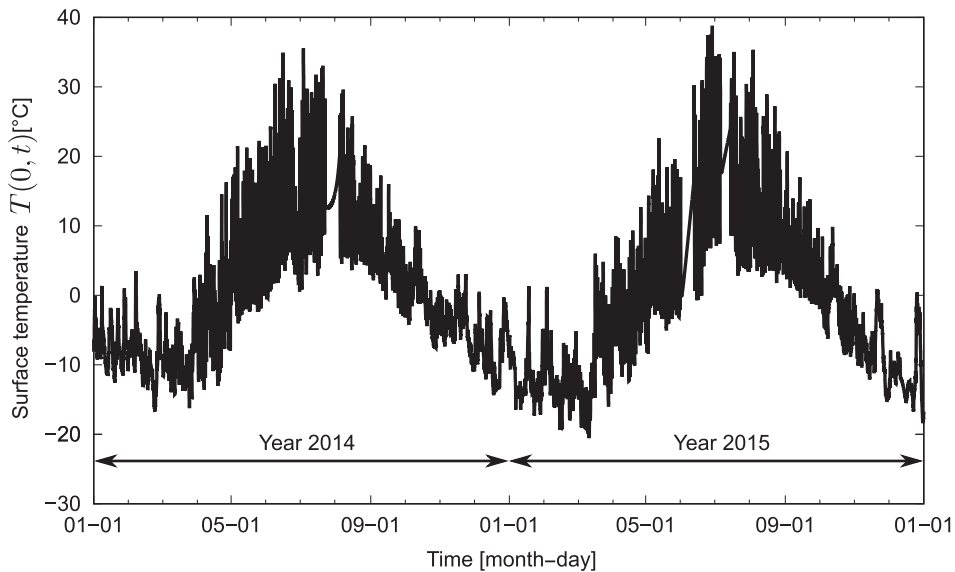

Fig. 5. Model-calculated surface temperature based on the 2014–2015 Nuuk weather data (see Fig. 4).

is linearly related to the temperature history (as expected). As a means of validation, the mechanical code was applied to measurements obtained in a thermal stress restrained specimen test. In the test, a mastic asphalt specimen with known thermo-viscoelastic properties was exposed to a cooling rate of $10\,°C \cdot h^{-1}$. The specimen was clamped at its ends, and stress build-up was recorded from an initial stress-free temperature of $20\,°C$ until failure at a temperature of $2\,°C$ (i.e., after 1.8 hours). The mechanical formulation was validated by attempting to reproduce the thermally-induced viscoelastic stress history measured in the test, which

varied from 0 MPa to a peak of -4.2 MPa (just before failure). After calibrating the material's linear thermal expansion coefficient, calculated stresses displayed near-perfect agreement with measurements, yielding a Pearson product-moment correlation coefficient of 0.998. The average absolute difference between calculated and measured stress values was 0.11 MPa (i.e., 2.6% of the peak).
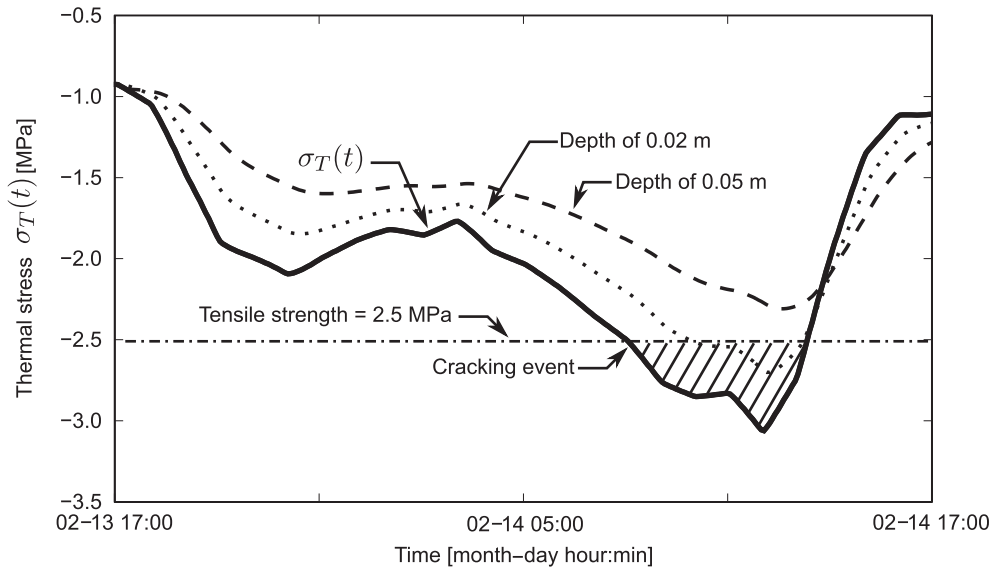
Fig. 6. Calculated surface thermal stress $\sigma_T(t)$ (solid line) and identification of a cracking event; near-surface stress buildup is shown for a depth of 0.02 m (dotted line) and a depth of 0.05 m (dashed line).

3. Numerical results

Thermomechanical calculations were carried out to identify a critical weather event leading to a build-up of thermal stresses exceeding Layer 1's tensile strength. Based on this critical event, calculations were repeated with the heating system being activated prior to the identified event. The calculations were split into two part: (*i*) simulation of a low-temperature cracking event, and (*ii*) assessment of heating activation.

3.1. Simulation of a low-temperature cracking event

Weather data from January 1st 2014 up to December 31st 2015 (both included) were utilized in the simulation. The data is presented in Fig. 4, which consists of four separate charts, depicting: air temperature, shortwave radiation, wind speed, and relative humidity. As can be seen, the air temperature ranged (approximately) from −15 °C to 15 °C. The shortwave radiation peaked at about 900 W·m^{-2}, and remained below 250 W·m^{-2} for about 263 days. The wind reached peak speed of

25 m·s^{-1} (i.e. 90 km·h^{-1}) and was on average 6 m·s^{-1} (i.e. 21.6 km·h^{-1}). The relative humidity remained consistently above 25%, with an average of 76%, and was above 95% for more than 42 days. Short periods of missing data occurred over the two years, lasting approximately ten days each. In order to apply the thermal formulation, the missing data were linearly interpolated.

Fig. 5 presents the calculated surface temperature history $T(0,t)$. The yearly variation of $T(0,t)$ can be observed, with temperature ranging between −20 °C to 40 °C. Minimal and maximal values occurred in March and in June/July, respectively. The surface temperature remained below 0 °C for about 411 days out of 729 days, i.e. about 56% of the time.

Based on the calculated surface temperature for January 2014 and onward, the mechanical formulation was applied to derive the thermal stress buildup at the surface of Layer 1. Fig. 6 presents the thermal stress history (solid line), focusing on a 24 h time interval during February 2015, starting from 17:00 on the 13th. The ordinate represents the calculated thermal stress, taken as negative for tensile conditions. As can
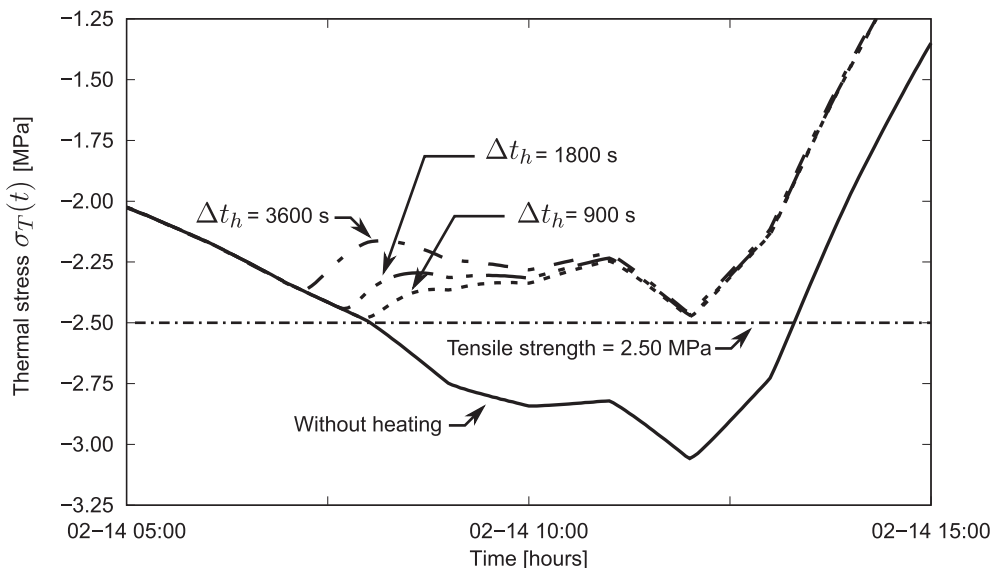

Fig. 7. Calculated thermal stress for three different time intervals of heating activation prior to identified cracking Δt_h.

be seen, this stress reached Layer 1's tensile strength of 2.5 MPa on February 14th at 08:02. During this weather event, the stress exceeded the strength for a period of 314 min (until 13:16); this period is indicated by the shaded area in the chart. It is the first time since the beginning of the thermomechanical analysis that the calculated tensile stress exceeded the tensile strength – indicating that low-temperature cracking would occur. This event is utilized hereafter to assess the effectiveness of heating activation in preventing cracking. In a separate side-study, the thermal stress buildup slightly below the surface of Layer 1 was calculated; the calculation results are included in Fig. 6 for a depth of 0.02 m (dashed line) and a depth of 0.05 m (dotted line). It can be seen that the strength is exceeded by the thermal stress also below the surface, but only after it had already been exceeded at the top. This behavior further substantiates the presumption that low-temperature cracking is a top-down phenomenon.

3.2. Assessment of heating activation

Thermomechanical calculations were repeated, this time with the internal heat source being activated prior to the identified low-temperature cracking event. For this purpose, the embedment depth as well as the heat production were fixed, with $z_r = 0.07$ m and $w_r = 200$ W·m^{-2}. The selected z_r represents a practical value of system installation depth that can enable future mill-and-overlay maintenance operations without damaging the system. The time interval of heating activation prior to the onset of cracking (i.e. first time the tensile strength is exceeded) is denoted by Δt_h. In example shown, the heating source was kept turned on from the time of Δt_h and to the end of the analysis. Fig. 7 presents the calculated thermal stress for the three different Δt_h values. It also presents the calculated thermal stress without heating (same as in Fig. 5). As can be seen, for $\Delta t_h = 900$ s, $\sigma_T(t)$ reached a maximal tensile stress value of 2.48 MPa, meaning that the low-temperature cracking would have been prevented from occurring. The larger Δt_h is, the smaller is the tensile stress peak; subsequently, for $\Delta t_h = 1800$ s and $\Delta t_h = 3600$ s, the low-temperature cracking would have been deterred as well. Furthermore, it can be seen that the three curves collapse into one, indicating that after some hours of heating the differences between the Δt_h are negligible. The increase in tensile stress seen after the collapse of the three curves, also reflected in the solid-line curve (without heating), is an effect of additional cooling of the pavement system. Heating generates an offset in $\sigma_T(t)$, reducing the tensile stress intensity; this reduction is not of constant value as it depends on the surface temperature history and on the asphalt concrete thermo-viscoelastic properties (and the heating system parameters).

Determined next is minΔt_h which denotes the minimal time interval of heating activation prior to the onset of cracking, i.e. the minimal time interval required to keep the calculated thermal stress below the tensile strength for the weather event in Fig. 6. This was done for six different embedment depths z_r combined with five different heat productions w_r. The embedment depths ranged from 0.05 m to 0.10 m, at 0.01 m increments, selected to represent a practical range for system installation. The heating production ranged from 200 W·m^{-2} to 300 W·m^{-2}, at

Table 2

Overview of minimal time interval of heating activation prior to the onset of cracking minΔt_h calculated for different embedment depths z_r and heat productions w_r.

minΔt_h [s]		Heat production w_r [W·m^{-2}]				
		200	225	250	275	300
Embedment depth z_r [m]	0.05	280	280	280	280	280
	0.06	400	400	380	380	380
	0.07	580	560	540	520	500
	0.08	3780	760	740	720	700
	0.09				960	940
	0.10				1280	1240

25 W·m^{-2} increments selected to represent a practical range for a heating output.

Table 2 presents the resulting minΔt_h values for the above cases. For the high-end heat production ($w_r = 300$ W·m^{-2}), minΔt_h is 280 s for an embedment depth of 0.05 m and 1240 s for an embedment depth of 0.10 m; i.e. about a fourfold increase in the minimal time interval required to prevent cracking with a mere 0.05 m increase in the system's embedment depth. A similar trend is seen for the low-end of heat production, where $w_r = 200$ W·m^{-2} is associated with a minΔt_h of 280 s for an embedment depth of 0.05 m and with 3780 s for an embedment depth of 0.08 m. The difference here in minΔt_h between the two depths is more than one order of magnitude. Missing values in Table 2 refer to combinations of z_r and w_r for which it was not possible for the heating system to prevent cracking – regardless of the activation duration prior to the event. This is because the increase of minΔt_h is nonlinear with the increase in z_r. For example, in the case of $w_r = 275$ W·m^{-2}, minΔt_h increases by 100 s (from 280 s to 380 s) as z_r increases by 1 cm (from 0.05 m to 0.06 m), while minΔt_h increases by 320 s (from 1280 s to 960 s) as z_r increases again by 1 cm (from 0.10 m to 0.09 m). Thus, the table demonstrates that deepening the heating system considerably diminishes its ability to control the stress buildup at the surface; conversely, placing the system closer to the surface considerably improves this ability. While not shown in the Table, a heat production of 300 W·m^{-2} was effective down to a depth of 0.15 m, and a heat production of $w_r = 275$ W·m^{-2} was effective down to a depth of 0.11 m.

4. Procedure for heating operation

An embedded electric heating system can potentially deter low-temperature cracking if it is activated at a time interval greater than minΔt_h. An automatic procedure to achieve this requires real-time monitoring of the surface thermal stress evolution ($\sigma_T(t)$), and activation of the heating system once a certain predefined stress threshold is exceeded. System deactivation can also be based on a similar approach – utilizing a stress threshold – which can be the same or different from the activation threshold. The utilization of a 1-D thermal model offers an advantage over more elaborate 2-D or 3-D schemes in terms of computational efficiency and hardware requirements. On the other hand, 1-D modeling cannot emulate the discrete nature of the heating system, and thus unable to capture the non-uniformity of surface temperature across the pavement's width. This modeling weakness must therefore be offset with a more conservative selection of a stress threshold.

As no sensor exists for measuring stresses, the required monitoring is only achievable based on the mechanical formulation – assuming the thermo-viscoelastic properties of the asphalt concrete are known – with the surface temperature history as input. The latter can be obtained in three different ways: (*i*) based on near-surface embedded sensors; (*ii*) from sensors embedded at larger depths, and employing some empirical transfer function to estimate the surface temperature history; and (*iii*) based on weather data from a nearby station (i.e. no embedded sensing) and applying the thermal formulation to calculate the surface temperature history.

The above activation procedure (based on calculated surface temperature from weather data) is hereafter demonstrated for the weather event in Fig. 6. This is done with an activation-deactivation stress threshold of 80% of Layer 1's tensile strength (i.e. $0.8 \cdot 2.5 = 2.00$ MPa). For preparing the demonstration, the system's embedment depth was fixed to $z_r = 0.07$ m and its heat production was fixed to $w_r = 200$ W·m^{-2}. Fig. 8 presents $\sigma_T(t)$ resulting from the chosen system activation procedure (solid line). Similar to Fig. 7, the chart spans ten hours; it includes two horizontal lines to graphically indicate the threshold and the tensile strength (dashed dotted line). As can be seen from the Figure, $\sigma_T(t)$ hovers around the threshold, then drops to a peak level of -2.44 MPa, after which it continues to increase. Thus, the tensile strength was not exceeded and therefore low-temperature
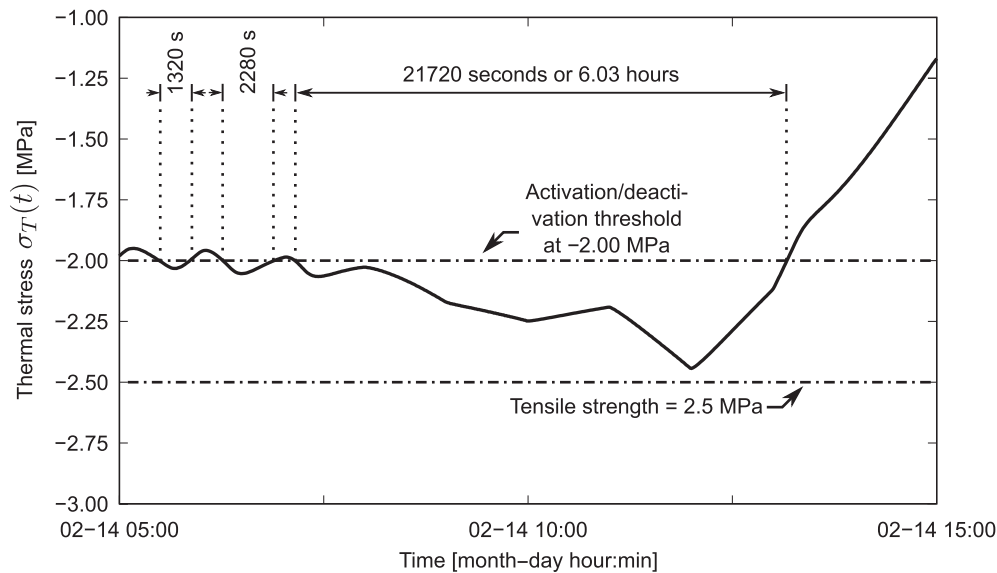
Fig. 8. Resulting $\sigma_T(t)$ (solid line) from the automatic procedure applied to Fig. 6's weather event with an activation/deactivation stress threshold at -2.00 MPa (dashed dotted line).

cracking avoided. Overall, the system was 'automatically' activated at three separate time intervals for which $\sigma_T(t)$ crossed the threshold. The total duration of activation was 25320 s, i.e. approximately 7.03 h.

5. Conclusion

This work addressed the case of an electrically heated asphalt pavement with ribbon elements. It explored an unconventional application of such a system – the mitigation of low-temperature cracking. The investigation included thermomechanical pavement modeling and measured weather data from Greenland (see Fig. 4). The thermal formulation (see Eq. (1) and Fig. 1) was 1-D, and considered external weather effects (e.g. solar, wind speed, etc.), an internal heat source representing an embedded heating system (smearing the effects of individual ribbons), and the effects of moisture freezing and thawing within a pavement layer. The mechanical formulation (see Eq. (16)) was based on linear viscoelasticity assuming thermo-rheological simplicity. After identifying a cold weather event that can cause cracking (see Fig. 6), a parametric investigation was carried out to assess the potential the heating system to mitigate the cracking (i.e. prevent its occurrence) – see Fig. 7 and Table 2. Lastly, a procedure was proposed and demonstrated for automatic heating operation based on a stress-threshold approach (see Fig. 8).

For the chosen input parameters (see Table 1), it was demonstrated that the overall idea of mitigating low-temperature cracking with an embedded electric heating system is attainable and workable. The thermomechanical modeling outlined in the work allows for quantifying the mitigation performance under any weather dataset, pavement properties, and heating system attributes. The parametric investigation showed that the ability to mitigate cracking is very sensitive to the system's embedment depth. To be effective, deeper systems require longer operational times and much higher heat production rates. For some depths, the required heat production becomes impractically high. The reason for this is the observation that low-temperature cracking is a top-down phenomenon, governed by the temperature history at the pavement surface that is directly exposed to weather effects (Canestrari and Ingrassia, 2020). The procedure suggested for automatic heating operation is deemed practical for real-life implementation, benefiting from the computational efficiency of 1-D thermal modeling.

Two potential benefits, not investigated in this work, include: (i) active mitigation of low-temperature fatigue cracking – caused by

several thermal stress cycles that ultimately produce a macro crack – even though each does not exceed the tensile strength. In this situation, operating an embedded heating system may delay such cracking or even completely deter it if stresses are actively kept below the so-called endurance limit (Hashin and Rotem, 1978); and (ii) active mitigation of damages due to frost action – caused by formation and volume expansion of ice lenses in frost-susceptible layers and subsequent settlements and loss of structural integrity during thawing periods. In this situation, operating an embedded heating system may slow or completely block the penetration of frost into the pavement. Both abovementioned benefits can be assessed with the thermal and mechanical formulations outlined in this work.

Declaration of Competing Interest

Acknowledgements

References

Adam, Q.F., 2021a. Heat transfer in a layered medium, github.com/QuentinFelixAdam/One-dimensional-thermal-code.

Adam, Q.F., 2021b. Thermally-induced stress history in a viscoelastic layer, github.com/QuentinFelixAdam/3D-Thermally-induced-linear-viscoelastic-stress.

American Society of Testing and Materials, 2020a. Standard practice for roads and parking lots pavement condition index surveys, ASTM D6433-20.

American Society of Testing and Materials, 2020b. Standard test method for airport pavement condition index surveys, ASTM D5340.

Andersland, O.B., Ladanyi, B., 2003. Frozen ground engineering, second ed. ASCE.

Apeagyei, A., Dave, E.V., Buttlar, W.G., 2008. Effect of cooling rate on thermal cracking of asphalt concrete pavements. Asph. Paving Technol.: Assoc. Asph. Paving Technol.-Proc. Tech. Sess. 77, 709–738.

Barber, E.S., 1957. Calculation of maximum pavement temperatures from weather reports. Bureau of Public Roads, Physical Research Branch.

Bentz, D.P., 2000. A computer model to predict the surface temperature and time-of-wetness of concrete pavements and bridge decks, Technical Report NISTIR 6551. National Institute of Standards and Technology, Technology Administration, U.S. Department of Commerce.

Bernd, M., 2010. Weak or strong: on coupled problems in continuum mechanics. Institut für Mechanik (Bauwesen), Lehrstuhl für Kontinuumsmechanik, Universität Stuttgart.

Bliss, R.W., 1961. Atmospheric radiation near the surface of the ground: a summary for engineers. Sol. Energy 5, 103–120.

Bolton, D., 1980. The computation of equivalent potential temperature. Mon. Weather Rev. 108, 1046–1053.

Canestrari, F., Ingrassia, L.P., 2020. A review of top-down cracking in asphalt pavements: causes, models, experimental tools and future challenges. J. Traffic Transp. Eng. (Engl. Ed.) 7, 541–572.

Cannon, J.R., 1984. The one-dimensional heat equation. Cambridge University Press, ISBN 9781139086967.

Cappelen, J., 2021. Weather observations from Greenland 1958–2020, Technical Report DMI Report 21–08. Danish Meteorological Institute https://www.dmi.dk/publikationer/, accessed on 7th April 2021, 2021.

Côté, J., Konrad, J.-M., 2005. Thermal conductivity of base-course materials. Can. Geotech. J. 42, 61–78.

Dempsey, J.B., Thompson, M.R., 1970. A heat-transfer model for evaluating frost action and temperature-related effects in multilayered pavement systems. In: Environmental effects on concrete, 49th Annual Meeting of the Highway Research Board. Washington District of Columbia, United States, pp. 39–56.

Dempsey, B.J., Herlache, W.A., Patel, A.J., 1986. Climatic-materials-structural pavement analysis program. Transp. Res. Rec. 111–123.

Duveiller, G., Fasbender, D., Meroni, M., 2016. Revisiting the concept of a symmetric index of agreement for continuous datasets. Sci. Rep. 6, 19401.

Findley, W.N., Lai, J.S.Y., 1967. A modified superposition principle applied to creep of nonlinear viscoelastic material under abrupt changes in state of combined stress. Trans. Soc. Rheol. 11, 361–380.

GEO-SLOPE International Ltd., 2014. Thermal modeling with TEMP/W, 1400, 633–6th Ave SW Calgary, Alberta, Canada T2P 2Y5.

Gudmarsson, A., Ryden, N., Di Benedetto, H., Sauzéat, C., 2015. Complex modulus and complex Poisson's ratio from cyclic and dynamic modal testing of asphalt concrete. Constr. Build. Mater. 88, 20–31.

Guymon, G.L., Hromadka II, T.V., Berg, R.L., 1984. Two dimensional model of coupled heat and moisture transport in frost-heaving soils. Trans. ASME 106, 336–343.

Hartmann, D.L., 1994. Chapter 4 The energy balance of the surface. In: Global Physical Climatology. International Geophysics, vol. 56. Academic Press, pp. 81–114.

Hashin, Z., Rotem, A., 1978. A cumulative damage theory of fatigue failure. Mater. Sci. Eng. 34, 147–160.

Hassn, A., Chiarelli, A., Dawson, A., Garcia, A., 2016. Thermal properties of asphalt pavements under dry and wet conditions. Mater. Des. 91, 432–439.

Hickson, R.I., Barry, S.I., Mercer, G.N., Sidhu, H.S., 2011. Finite difference schemes for multilayer diffusion. Math. Comput. Modell. 54, 210–220.

Hills, J.F., Brien, D., 1966. The fracture of bitumens and asphalt mixes by temperature induced stress. Proc. Assoc. Asph. Paving Technol. 35, 292–309.

Islam, M., Tarefder, R., 2015. Coefficients of thermal contraction and expansion of asphalt concrete in the laboratory. J. Mater. Civ. Eng. 27, 04015020-1–04015020-8.

Janke, B.D., Herb, W.R., Mohseni, O., Stefan, H.G., 2009. Simulation of heat export by rainfall-runoff from a paved surface. J. Hydrol. 365, 195–212.

Johnston, G.H., 1981. Permafrost engineering design and construction. Wiley, Toronto.

Judycki, J., Jaskula, P., Dolzycki, B., Pszczola, M., Jaczewski, M., Rys, D., Stienss, M., 2015. Investigation of low-temperature cracking in newly constructed high-modulus asphalt concrete base course of a motorway pavement. Road Mater. Pavement Des. 16, 362–388.

Kirchhoff, G., 1860. Über das verhältniss zwischen dem emissionsvermögen und dem absorptionsvermögen der körper für wärme und licht. Ann. Phys. Chem. 185, 275–301.

Kliewer, J.E., Zeng, H., Vinson, T.S., 1996. Aging and low-temperature cracking of asphalt concrete mixture. J. Cold Reg. Eng. 10, 134–148.

Lawrence, M.G., 2005. The relationship between relative humidity and the dewpoint temperature in moist air: a simple conversion and applications. Bull. Am. Meteorol. Soc. 86, 225–234.

Lawrence, I., Lin, K., 1989. A concordance correlation coefficient to evaluate reproducibility. Biometrics 255–268.

Levenberg, E., Adam, Q.F., 2021. Construction of an electrically heated asphalt road based on ribbon technology. Transp. Res. Rec. 2675, 652–663.

Ling, M., Luo, X., Gu, F., Lytton, R.L., 2017. Time-temperature-aging-depth shift functions for dynamic modulus master curves of asphalt mixtures. Constr. Build. Mater. 157, 943–951.

Liu, H., Luo, R., 2017. Development of master curve models complying with linear viscoelastic theory for complex moduli of asphalt mixtures with improved accuracy. Constr. Build. Mater. 152, 259–268.

Liu, K., Huang, S., Jin, C., Xie, H., Wang, F., 2017. Prediction models of the thermal field on ice-snow melting pavement with electric heating pipes. Appl. Therm. Eng. 120, 269–276.

Liu, K., Zhang, X., Guo, D., Wang, F., Xie, H., 2018. The interlaminar shear failure characteristics of asphalt pavement coupled heating cables. Mater. Struct. 51, 1–13.

Magnus, G., 1844. Versuche über die Spannkräfte des Wasserdampfs. Ann. Phys. 137, 225–247.

Marasteanu, M.O., Li, X., Clyne, T.R., Voller, V.R., Timm, D.H., Newcomb, D.E., 2004. Low temperature cracking of asphalt concrete pavements, techreport MN/RC. University of Minnesota.

Marasteanu, M., Moon, K.H., Teshale, E.Z., Falchetto, A.C., Turos, M., Buttlar, W., Dave, E.V., Paulino, G., Ahmed, S., Leon, S., Breaham, A., Behnia, B., Bahia, H., Tabatabaee, H., Velasquez, R., Arshadi, A., Puchalski, S., Mangiafico, S., Williams, C., Buss, A., Bausano, J., Kvasnak, A., 2007. Investigation of low temperature cracking in asphalt pavements national pooled fund study - phase II, Technical Report MN/RC 2012-23. Minnesota Department of Transportation.

McCullough, B.F., Rasmussen, R.O., 1999. Fast-track paving: concrete temperature conctrol and traffic opening criteria for bonded concrete overlays Volume I: Final report, Technical Report FHWA-RD-98-167. Transec Inc.

Morland, L.W., Lee, E.H., 1960. Stress analysis for linear viscoelastic materials with temperature variation. Trans. Soc. Rheol. 4, 233–263.

National Academies of Sciences, Engineering, and Medicine, 2010. Top-down cracking of hot-mix asphalt layers: models for initiation and propagation, Technical Report. The National Academies Press, Washington, DC.

National Academies of Sciences, Engineering, and Medicine, 2018. A mechanistic empirical model for top down cracking of asphalt pavements layers, Technical Report. The National Academies Press, Washington, DC.

Newton, I., 1701. Scala graduum caloris, Calorum descriptiones & signa (scale of the degrees of heat). Philos. Trans. 22, 824–829.

Nicolsky, D.J., Romanovsky, V.E., Panteleev, G.G., 2009. Estimation of soil thermal properties using in-situ temperature measurements in the active layer and permafrost. Cold Reg. Sci. Technol. 55, 120–129.

Rew, Y., Shi, X., Choi, K., Park, P., 2018. Structural design and lifecycle assessment of heated pavement using conductive asphalt. J. Infrastruct. Syst. 24.

Richard, Y.K., 2009. Modeling of Asphalt Concrete, Chapter 1: Modeling of Asphalt Concrete. American Society of Civil Engineers.

Sangiorgi, C., Settimi, C., Tataranni, P., Lantieri, C., Adomako, S., 2018. Thermal analysis of asphalt concrete pavements heated with amorphous metal technology. Adv. Mater. Sci. Eng. 2018, 1–8.

Schindler, A.K., Ruiz, J.M., Rasmussen, R.O., Chang, G.K., Wathne, L.G., 2004. Concrete pavement temperature prediction and case studies with the FHWA HIPERPAV models. Cem. Concr. Compos. 26, 463–471.

Schwarzl, F., Staverman, A.J., 1952. Time-temperature dependence of linear viscoelastic behavior. J. Appl. Phys. 23, 838–843.

Solaimanian, M., Kennedy, T.W., 1993. Predicting maximum pavement surface temperature using maximum air temperature and hourly solar radiation. Transp. Res. Rec. 1–11.

Sorvari, J., Hämäläinen, J., 2010. Time integration in linear viscoelasticity – a comparative study. Mech. Time-Depend. Mater. 14, 307–328.

Van Buren, M.A., Watt, W.E., Marsalek, J., Anderson, B.C., 2000. Thermal enhancement of stormwater runoff by paved surfaces. Water Res. 34, 1359–1371.

Vehrencamp, J.E., 1953. Experimental investigation of heat transfer at an air-earth interface. Trans. Am. Geophys. Union 34, 22–30.

Wang, H., 2018. Investigation on the mechanisms of block cracking in asphalt pavements. PhD thesis. University of Illinois at Urbana-Champaign.

Wang, H., Roesler, J., Guo, D.-Z., 2009. Analytical approach to predicting temperature fields in multi-layered pavement systems. J. Eng. Mech. 135, 334–344.

Wexler, A., 1976. Vapor pressure formulation for water in range 0 to 100 °C. A revision. J. Res. Natl. Bur. Stand. Sect. A Phys. Chem. 80A, 775–785.

Williams, M.L., Landel, R.F., Ferry, J.D., 1955. The temperature dependence of relaxation mechanisms in amorphous polymers and other glass-forming liquids. J. Am. Chem. Soc. 77, 3701–3707.

Wolfe, W.L., 1965. Handbook of military infrared technology.

Wolfe, R.K., Heath, G.L., Colony, D.C., 1983. Cooling curve prediction of asphaltic concrete. J. Transp. Pipeline Eng. 109, 137–147.

Zhang, Y., Rossow, W.B., Lacis, A.A., Oinas, V., Mishchenko, M.I., 2004. Calculation of radiative fluxes from the surface to top of atmosphere based on ISCCP and other global data sets: Refinements of the radiative transfer model and the input data. J. Geophys. Res. 109, 1–27.

Zhang, M., Zhang, X., Lu, J., Pei, W., Wang, C., 2019. Analysis of volumetric unfrozen water contents in freezing soils. Exp. Heat Transf. 32, 426–438.